



HAL
open science

A heliospheric density and magnetic field model

G. Mann, A. Warmuth, C. Vocks, A. P. Rouillard

► **To cite this version:**

G. Mann, A. Warmuth, C. Vocks, A. P. Rouillard. A heliospheric density and magnetic field model. Astronomy and Astrophysics - A&A, 2023, 679, 10.1051/0004-6361/202245050 . insu-04473141

HAL Id: insu-04473141

<https://insu.hal.science/insu-04473141>

Submitted on 23 Feb 2024

HAL is a multi-disciplinary open access archive for the deposit and dissemination of scientific research documents, whether they are published or not. The documents may come from teaching and research institutions in France or abroad, or from public or private research centers.

L'archive ouverte pluridisciplinaire **HAL**, est destinée au dépôt et à la diffusion de documents scientifiques de niveau recherche, publiés ou non, émanant des établissements d'enseignement et de recherche français ou étrangers, des laboratoires publics ou privés.



Distributed under a Creative Commons Attribution 4.0 International License

A heliospheric density and magnetic field model[★]

G. Mann¹, A. Warmuth¹, C. Vocks¹, and A. P. Rouillard^{2,3}

¹ Leibniz-Institut für Astrophysik Potsdam (AIP), An der Sternwarte 16, 14482 Potsdam, Germany
e-mail: GMann@aip.de

² Institut de Recherche en Astrophysique et Planétologie, Université de Toulouse III (UPS), 14 av. Édouard Belin, 31400 Toulouse, France

³ Centre National de la Recherche Scientifique, UMR 5277, Université Paul Sabatier, 9 av. du Colonel Roche, 31028 Toulouse, France

Received 23 September 2022 / Accepted 23 August 2023

ABSTRACT

Context. The radial evolution of the density of the plasma and the magnetic field in the heliosphere, especially in the region between the solar corona and the Earth's orbit, has been a topic of active research for several decades. Both remote-sensing observations and in situ measurements by spacecraft such as HELIOS, Ulysses, and WIND have provided critical data on this subject. The NASA space mission Parker Solar Probe (PSP), which will approach the Sun down to a distance of 9.9 solar radii on December 24, 2024, gives new insights into the structure of the plasma density and magnetic field in the heliosphere, especially in the near-Sun interplanetary space. This region is of particular interest because the launch and evolution of coronal mass ejections (CMEs), which can influence the environment of our Earth (usually called space weather), takes place there.

Aims. Because of the new data from PSP, it is time to revisit the subject of the radial evolution of the plasma density and magnetic field in the heliosphere. To do this, we derive a radial heliospheric density and magnetic field model in the vicinity of the ecliptic plane above quiet equatorial regions. The model agrees well with the measurements in the sense of a global long-term average.

Methods. The radial evolution of the density and solar wind velocity is described in terms of Parker's wind equation. A special solution of this equation includes two integration constants that are fitted by the measurements. For the magnetic field, we employed a previous model in which the magnetic field is described by a superposition of the magnetic fields of a dipole and a quadrupole of the quiet Sun and a current sheet in the heliosphere.

Results. We find the radial evolution of the electron and proton number density as well as the radial component of the magnetic field and the total field strength in the heliosphere from the bottom of the corona up to a heliocentric distance of 250 solar radii. The modelled values are consistent with coronal observations, measurements at 1 AU, and with the recent data from the inner heliosphere provided by PSP.

Conclusions. With the knowledge of the radial evolution of the plasma density and the magnetic field in the heliosphere the radial behaviour of the local Alfvén speed can be calculated. It can reach a local maximum of 392 km s^{-1} at a distance of approximately 4 solar radii, and it exceeds the local solar wind speed at distances in the range of 3.6–13.7 solar radii from the centre of the Sun.

Key words. Sun: corona – Sun: heliosphere – Sun: magnetic fields – solar-terrestrial relations – solar wind

1. Introduction

The permanent flow of plasma produced by the solar corona, called solar wind, fills the entire heliosphere. The behaviour of the density and the magnetic field in the heliosphere, especially in the region between the corona and the Earth's orbit, is of great scientific interest. Coronal mass ejections (CMEs) are launched in the solar corona, evolve in near-Sun interplanetary space, and travel through the heliosphere. If they impinge on the Earth's magnetosphere, they influence the environment of our Earth. This effect is usually called space weather. For instance, in order to predict the transit time of a CME from the Sun to the Earth, the knowledge of the density behaviour in the region between the corona and the Earth is important because CMEs interact with the background solar wind flow (Vršnak et al. 2013). This shows that a model of the density and magnetic field in the heliosphere is important.

For several decades, the variation in the density and magnetic field with heliocentric distance has been studied intensively in different ways with ground-based and space-borne measurements. Coronal densities were measured

- from white-light coronagraphic observations (see e.g. Baumbach 1937; Van de Hulst 1950; Newkirk 1961; Saito et al. 1977; Leblanc et al. 1973; Koutchmy & Livshits 1992; Koutchmy 1994), assuming the polarized brightness of white light to be generated by Thomson scattering,
- by means of the emission measure deduced from space-borne extreme-UV (EUV) and X-ray measurements (see e.g. Aschwanden et al. 1999; Zucca et al. 2014),
- by means of the scintillation of radio sources (see e.g. Erickson 1964; Bird & Edenhofer 1990), and
- with space-borne in situ instruments OGO-5 (Alvarez & Haddock 1973), HELIOS (Bougeret et al. 1984; Schwenn 1990), ULYSSES (Issautier et al. 1997), WIND (Leblanc et al. 1998), COR2 on board STEREO (Morgan 2021), SWAVES on board STEREO, and FIELDS on board PSP (Badman et al. 2022).

The coronal and interplanetary magnetic fields have also been studied

- by evaluation of solar radio bursts (see e.g. Dulk & McLean 1978),
- by Faraday rotation measurements (see e.g. Bird & Edenhofer 1990 as a review),
- by remote-sensing observations (e.g. with the Coronal Multi-channel Polarimeter, Yang et al. 2020), and

* Full Table 8 is available at the CDS via anonymous ftp to cdsarc.cds.unistra.fr (130.79.128.5) or via <https://cdsarc.cds.unistra.fr/viz-bin/cat/J/A+A/679/A64>

– by space-borne in situ measurements (e.g. by HELIOS, Mariani & Neubauer 1990, Bird et al. 1994; ULYSSES, Balogh et al. 1995; and PSP, Horbury et al. 2020; Kasper et al. 2021).

Owens & Forsyth (2013) provide a useful review of this topic.

Mann et al. (1999a) introduced a heliospheric density model that describes the density fall-off with heliocentric radial distance up to 5 astronomical units (AU). This model was consistent with the in situ measurements available at the time. The model was based on a special solution of Parker (1958) wind equation.

Meanwhile, new relevant data have become available, especially from the NASA Parker Solar Probe (PSP) mission. PSP was launched on August 12, 2018. It travels in a highly elliptical orbit around the Sun and is scheduled to approach the Sun to a distance of $9.9 R_{\odot}$ (R_{\odot} , solar radius) on December 24, 2024¹. This mission provides new insights into the plasma conditions in the inner heliosphere, especially in near-Sun interplanetary space. Hence, it is time to revisit the radial evolution of the plasma density and magnetic field in the inner heliosphere.

The aim of this paper is to develop a model describing the radial evolution of the electron and proton number density (N_e and N_p , respectively), the solar wind (or proton) speed (v_p), the radial component of the magnetic field (B_r) as well as the total field strength (B_{tot}), and the radial profile of the local Alfvén speed (v_A) in the vicinity of the ecliptic plane above quiet equatorial regions in the distance range of 1–250 R_{\odot} (1 AU = 215 R_{\odot}) in the sense of a long-term average global model.

In Sect. 2 we summarize and evaluate the data available from ground-based and space-borne measurements, especially from PSP. The radial evolution of the electron (or proton) number density and the solar wind speed is derived by employing Parker’s wind equation in Sect. 3. The global magnetic field model by Banaszek et al. (1998) is adopted to describe the spatial evolution of the magnetic field in the vicinity of the ecliptic plane above quiet equatorial regions in Sect. 4. With the knowledge of the radial evolution of the proton number density (see Sect. 3) and the magnetic field (see Sect. 4), the radial evolution of the local Alfvén speed is calculated in Sect. 5, where the results of the paper are also discussed. The paper concludes with a summary (Sect. 6).

2. Density and magnetic field data in the heliosphere

In the following, we present a summary of the known data of the density, solar wind velocity, and magnetic field in the corona and heliosphere.

Figure 1 shows the radial evolution of coronal electron number density in the range 1–2 R_{\odot} as obtained from the various studies listed in Table 1. All measurements that are considered here were obtained for quiet equatorial regions. We determined the electron densities at the base of the corona by extrapolation to $r = 1 R_{\odot}$, also given in Table 1. The base of the corona is defined as the level at which the temperature exceeds 1×10^6 K, so that the plasma is fully ionized. This occurs at about 3 Mm above the photosphere (see Fig. 1.2 in Priest 1982). Hence, the bottom of the corona is located at a radial distance of $1.0043 R_{\odot} \approx 1 R_{\odot}$. The table reveals that the electron number density can vary by about an order of magnitude at the bottom of the corona. Therefore, the mean value of $N_e = 7.42 \times 10^8 \text{ cm}^{-3}$ was adopted as a representative one of the electron number density at the bottom of the corona above quiet equatorial regions.

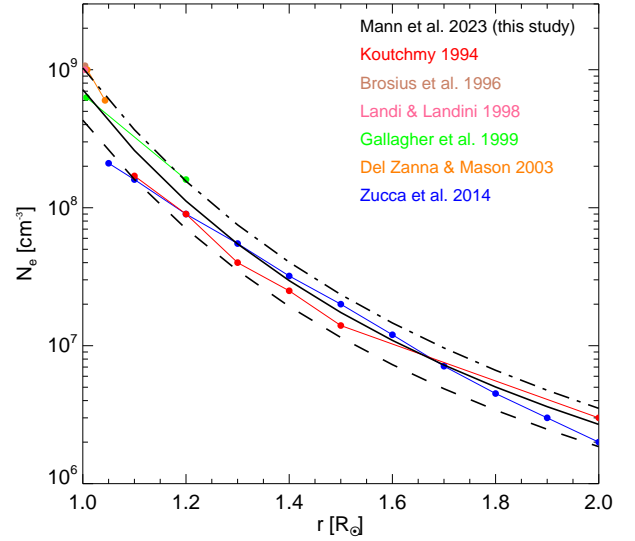


Fig. 1. Radial evolution of the electron number density N_e above quiet equatorial regions in the solar corona. Observational results from different studies are compared to the model developed in this study (black curve).

Table 1. Electron number densities $N_e(r = R_{\odot})$ at the bottom of the corona above quiet equatorial regions.

Paper	N_e [cm^{-3}]
Newkirk (1961)	8.78×10^8
Koutchmy (1994)	3.59×10^8
Brosius et al. (1996)	1.09×10^9
Landi & Landini (1998)	9.75×10^8
Gallagher et al. (1999)	6.64×10^8
Del Zanna & Mason (2003)	9.75×10^8
Zucca et al. (2014)	2.73×10^8
Geometric mean	7.42×10^8

In situ spacecraft measurements of the heliospheric electron number density N_e , the radial proton (or solar wind) speed v_p , the proton flux $N_p v_p$, and the constant $C_p = N_p v_p r^2$ are summarized in Table 2. The values in Table 2 were derived from the measurements obtained with the Solar Wind Electron, Alphas, and Protons (SWEAP) instrument (Kasper et al. 2016) on board PSP by combining the data from encounters one through nine. Specifically, we used the hourly averaged data provided in the PSP_COHO1HR_MERGED_MAG_PLASMA data product obtained from the CDAWeb website² where N_p and v_p were derived from 1D Maxwellian fits of high-resolution SWEAP data taken by the Solar Probe Cup (SPC), a Faraday-cup instrument that is directly pointed at the Sun and measures both ions and electrons. In this study, we only considered density measurements made by SPC at heliospheric radial distances greater than $20 R_{\odot}$ because closer to the Sun, the solar wind beam is not always recorded comprehensively due to the spacecraft motion, and the SPAN-i instrument should then also be considered for ion densities. The electron density N_e (which is discussed in Sect. 5) was derived from the instrument FIELDS (Bale et al. 2016) on board PSP using quasi-thermal noise

¹ See <https://sppgway.jhuapl.edu/encounters>

² See <https://cdaweb.gsfc.nasa.gov>

Table 2. Mean values and standard derivation of the electron number density N_e , the proton (or solar wind) speed v_p , and $C_p = N_p v_p r^2$ as given by the SWEAP instrument on board PSP at 30, 50, and 70 R_\odot as well as by the OMNI database at 1 AU ($=215 R_\odot$).

Parameter	r/R_\odot	Source	Value
N_e [cm^{-3}]	1	Table 1	$(7.42 \pm 3.18) \times 10^8$
	30	PSP	676 ± 332
	50	PSP	222 ± 73
	70	PSP	157 ± 39
	215	OMNI	7.26 ± 3.71
v_p [km s^{-1}]	30	PSP	308 ± 73
	50	PSP	306 ± 39
	70	PSP	328 ± 79
	215	OMNI	390 ± 84
C_p [10^{34} s^{-1}]	30	PSP	7.18 ± 73
	50	PSP	8.57 ± 5.63
	70	PSP	6.69 ± 1.95
	215	OMNI	5.05 ± 2.4

Notes. Here, OMNI data are used only during PSP times. The values of the electron number density at the coronal base are determined by means of the data given in Table 1.

spectroscopy³ (see Moncuquet et al. 2020) during encounters E1–E10. We used one-hour averages of N_e in order to be consistent with the SWEAP data. The total distance range that is covered by PSP data is 13.3–129.3 R_\odot . Measurements at 1 AU were provided by the OMNI database (Papitashvili & King 2020), which combines proton data from the 3DP instrument (Lin et al. 1995) on board Wind and from SWEPAM (Stone et al. 1998) on board ACE. Here, we averaged the daily OMNI data over the period of 2018–2021.

Figure 2 shows the values of C_p measured by PSP in the range 20–130 R_\odot during its orbits E1–E9. The PSP data show that even inside heliospheric radial distances of 40 R_\odot , proton densities can vary by nearly an order of magnitude. This is likely the result of the spacecraft passing through a range of solar wind structures that originated in different coronal source regions such as helmet streamers (Rouillard et al. 2020), isolated corona holes (Gritton et al. 2021), and pseudo-streamers (Kasper et al. 2021). The quantity C_p should be a conserved quantity because of the equation of continuity (see the discussion in Sect. 3). Table 2 provides $6.87 \times 10^{34} \text{ s}^{-1}$ for the mean value of C_p , which is drawn as the horizontal line in Fig. 2, revealing that a value like this is justified to be considered as being representative for C_p . C_p varies strongly because the heliosphere is not a homogeneous medium, but is structured spatially and temporally. For instance, there are fast and slow solar wind streams, coronal holes, coronal mass ejections (CMEs), and corotating interaction regions (CIR; see Priest 1982; Aschwanden 2005; Schwenn 1990).

The heliospheric plasma is assumed to be composed of electrons (e), protons (p), and double-ionized helium (He^{++}) with the particle number densities N_e , N_p , and N_{He} (as considered in Mann et al. 1999a), respectively. Then, the mass density d is given by

$$d = m_e N_e + m_p N_p + m_{\text{He}} N_{\text{He}} = \tilde{\mu} m_p N \quad (1)$$

(m_e is the electron mass, m_p is the proton mass, and $m_{\text{He}} = 4m_p$ is the helium mass) with the mean molecular weight $\tilde{\mu}$ and the

³ SQTN L3 data were obtained from <https://cdpp-archive.cnes.fr>

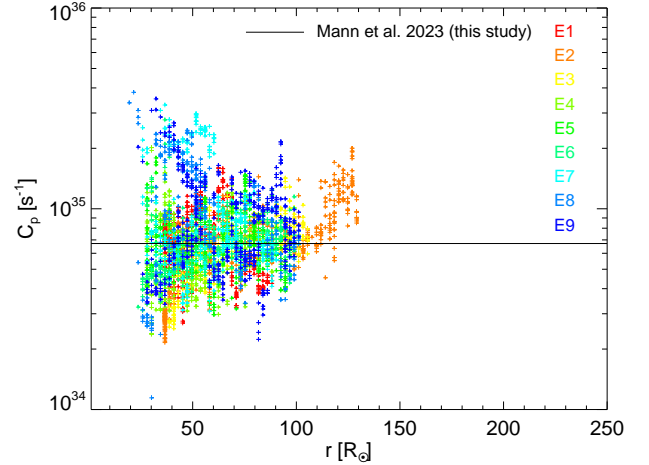


Fig. 2. Quantity $C_p = N_p v_p r^2$ as a function of heliocentric distance r . The crosses show C_p as measured by the SWEAP instrument during PSP encounters E1–E9 (colour-coded as indicated at the right). The full line corresponds to $C_p = 6.71 \times 10^{34} \text{ s}^{-1}$.

full particle number density $N = N_e + N_p + N_{\text{He}}$. The charge neutrality requires

$$N_e = N_p + 2N_{\text{He}} = (1 + 2\nu)N_p, \quad (2)$$

with $\nu = N_{\text{He}}/N_p$. Because of $m_e \ll m_p$, we obtain

$$d = (1 + 4\nu) \cdot m_p N_p. \quad (3)$$

Equations (1)–(3) lead to the relations

$$N_e = (1 + 2\nu) \cdot N_p = \frac{(1 + 2\nu)}{(2 + 3\nu)} \cdot N \quad (4)$$

and

$$N_p = \frac{1}{(2 + 3\nu)} \cdot N, \quad (5)$$

with

$$\tilde{\mu} = \frac{(1 + 4\nu)}{(2 + 3\nu)}. \quad (6)$$

The ratio ν has typical values of 0.085 (see Tables 2 and 1.2 in Aschwanden 2005) and 0.0316 (see Fig. 3.22 in Schwenn 1990) in the corona and in the heliosphere at 1 AU. Hence, the mean value of 0.058 can be considered as typical for the ratio ν , leading to $\tilde{\mu} = 0.57$, $N_e = 1.12 N_p$ (or $N_p = 0.9 N_e$), $N_e = 0.51 N$ (or $N = 1.95 N_e$) by means of Eqs. (4)–(6). Furthermore, in situ measurements at 1 AU provide $N_e = 1.063 N_p = 0.507 N$.

Leblanc et al. (1998) derived an electron density model of the region between the corona and the Earth’s orbit in the ecliptic plane. They exploited type III radio bursts recorded in the range 13.8 MHz down to a few kHz with the WAVES instruments (Bougeret et al. 1995) on board the Wind spacecraft. Type III radio bursts (Wild 1950) are considered the radio signatures of beams of energetic electrons (see Reid & Ratcliffe 2014 as a review). These electrons are generated in the solar corona and travel along magnetic field lines from the corona into the interplanetary space. They can be observed in situ by the 3D plasma instrument (Lin et al. 1995) onboard the Wind spacecraft, for instance, when they impact the spacecraft. This method tracks the propagation of electron beams, and as they trigger radio emission at the local plasma frequency, which can be used to

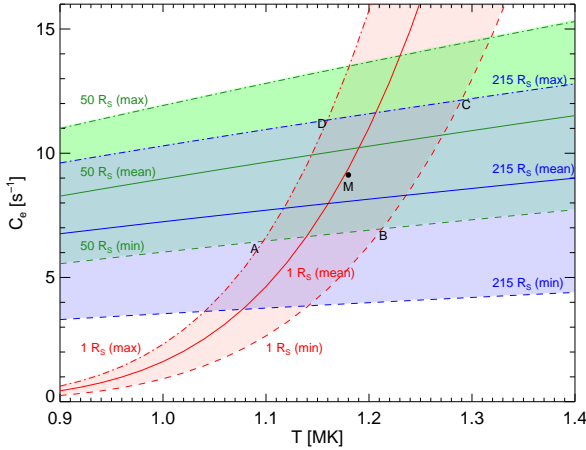


Fig. 3. Dependence of C_e on the temperature T for the mean (full lines), minimum (dashed lines), and maximum (dash-dotted lines) case of the electron number density N_e , and for $R = 1$ (red), 50 (green), and 215 (blue).

Table 3. Mean values and standard deviation of the radial component of the magnetic field B_r and of the total magnetic field strength B_{tot} as given by the instrument FIELDS on board PSP at 30, 50, and 70 R_\odot as well as by the OMNI database at 1 AU.

r/R_\odot	B_r [nT]	B_{tot} [nT]
30	86 ± 34.9	91.9 ± 32.7
50	31.8 ± 13.9	39.6 ± 10.8
70	15.2 ± 9.3	19.4 ± 8.5
215	1.56 ± 1.03	4.42 ± 1.39

infer the local electron density. As a result, Leblanc et al. (1998) found an empirical formula of the radial dependence on the electron number density $N_e(r)$ given in cm^{-3} ,

$$N_e(r) = \frac{3.3 \times 10^5}{R^2} + \frac{4.1 \times 10^6}{R^4} + \frac{8.0 \times 10^7}{R^6} \quad (7)$$

with $R = r/R_\odot$ providing $N_e = 7.14 \text{ cm}^{-3}$ at 1 AU. Equation (7) is very consistent with the observations (as shown in Fig. 5 in Leblanc et al. 1998). $N_e(r)$ according to Eq. (7) is indicated as the dashed line in Fig. 3. We compare Leblanc's model to our model and to the PSP data in Sect. 5.

After addressing the plasma densities, we now discuss magnetic field strengths in the heliosphere. In interplanetary space, the radial dependence of the magnetic field was derived by means of Faraday rotation measurements with the so-called coronal sounding experiment (Porsche 1977) on board Helios (see e.g. Bird & Edenhofer 1990 for a review) in the range $1.02 \leq R \leq 20$ (Pätzold et al. 1987) and by in situ measurements at $R \geq 62$ (Mariani & Neubauer 1990). The empirical formula

$$B_r(r) = \frac{6}{R^3} + \frac{1.18}{R^2} \quad (8)$$

fits both observations well. Here, B_r is given in Gauss (G) ($1 \text{ G} = 10^{-4} \text{ T} = 10^5 \text{ nT}$; $1 \text{ nT} = 10^{-5} \text{ G}$). Equation (9) provides a radial magnetic field strength of 2.55 nT at 1 AU.

In situ spacecraft measurements of the magnetic field are summarized in Table 3. We provide mean values for the radial component of the magnetic field B_r and the

total magnetic field strength B_{tot} . At 30, 50, and 70 R_\odot , these parameters were obtained from the instrument FIELDS (Bale et al. 2016) on board PSP by averaging over encounters E1–E9. Again, we used the hourly averaged data provided in the PSP_COHO1HR_MERGED_MAG_PLASMA data product, which include the FIELDS Fluxgate Magnetometer data. At 1 AU, the quantities were derived from the OMNI database (Papitashvili & King 2020), which combines magnetic field data from the instruments WAVES (Bougeret et al. 1995) on board Wind and MAG (Stone et al. 1998) on board ACE. Again, the daily OMNI values were averaged over the period of 2018–2021.

The observational data summarized in this section were used to search for a heliospheric density and magnetic field model that provides a good fit to the observations.

3. Heliospheric density model

Mann et al. (1999a) introduced a heliospheric density model based on a special solution of Parker (1958) wind equation (see Eq. (8) in Mann et al. 1999a),

$$v'(r)^2 - \ln(v'(r)^2) = 4 \cdot \ln(r') + \frac{4}{r'} - 3, \quad (9)$$

with $v'(r) = v(r)/v_c$ (critical velocity $v_c = (k_B T / \tilde{\mu} m_p)^{1/2}$) and $r' = r/r_c$ (critical radius $r_c = \gamma_G M_\odot / 2 v_c^2$) (k_B is Boltzmann's constant, T is the temperature, m_p is the proton mass, γ_G is the gravitational constant, and M_\odot is the mass of the Sun). It was derived from the stationary spherically symmetric magnetohydrodynamic equations supplemented by the isothermal equation of state (see Priest 1982), that is, the temperature T was considered to be constant in the whole heliosphere. The equation of continuity of the particle species i ($i = e$ for electrons and $i = p$ for protons; see Priest 1982) provides

$$r'^2 \cdot N'_i(r) \cdot v'(r) = 1, \quad (10)$$

with $N'_i(r) = N_i(r)/N_{i,c}$ (see Eq. (7) in Mann et al. 1999a) and $r_c^2 \cdot N_{c,i} \cdot v_c = C_i$. At the critical radius r_c , the particle number density N_i of the species i and the solar wind velocity have the values $N_{i,c}$ and v_c , respectively. Thus, Eqs. (9) and (10) provide the radial behaviour of the number density $N_i(r)$ of the particle species i and the solar wind (or proton) velocity $v(r)$. Equations (9) and (10) have two constants that completely determine the solutions, namely the critical velocity v_c (or the temperature T) and the constant C_i . Basically, Parker's wind Eq. (9) results from a one-fluid approach for describing a plasma. The electron number density is derived from the full particle number density by Eq. (4) taking the composition of the heliospheric plasma into account.

In the near-Sun region, that is, at $r \ll r_c$, the solar wind velocity is low, that is, $v \ll v_c$. Under this condition, Eqs. (9) and (10) are reduced to

$$N_i(r) = N_{i,\odot} \cdot \exp\left(\frac{2 r_c}{R_\odot} \cdot \left[\frac{R_\odot}{r} - 1\right]\right), \quad (11)$$

with $N_{i,\odot} = N_{i,c} \cdot \exp([2 r_c / R_\odot] - 3/2)$ as the particle number density of the species i at the bottom of the corona, that is, $r = R_\odot$.

The aim is to find the radial dependence of the electron number density and the solar wind (or proton) speed in the inner heliosphere, that is, in the range 1–250 R_\odot . In order to do this, we searched the solutions of Eqs. (9) and (10) that agree best with the observations given in Table 2. This was done in the following manner:

Table 4. Standard variation of the electron number densities N_e at $r/R_\odot = 1, 50,$ and 215 according to Table 2.

r/R_\odot	Min (N_e) [cm ⁻³]	Mean (N_e) [cm ⁻³]	Max (N_e) [cm ⁻³]
1	4.24×10^8	7.42×10^8	10.6×10^8
50	149	222	295
215	3.55	7.26	10.97

Table 5. Values of T and C_e for points A, B, C, D, and M (see Fig. 3), and the corresponding values of the critical velocity v_c and radius r_c .

Point	T [MK]	C_e [10 ³⁴ s ⁻¹]	v_c [km s ⁻¹]	r_c [Mm]
A	1.10	6.496	126.2	4158
B	1.21	6.925	132.3	3784
C	1.28	11.82	131.1	3575
D	1.14	11.32	129.6	3943
M	1.18	9.127	130.7	3877

- Equation (9) was solved for temperatures in the range 0.9–1.4 MK. The result was a function of the solar wind (or proton) velocity depending on radial distance $R (=r/R_\odot)$ and temperature T .
- As shown in Table 2, the values of the electron number density and the solar wind speed vary over a wide range. Therefore, we took these variations into account in the further treatment. Then, the minimum, mean, and maximum values of $C_e = r^2 N_e v(r)$ were calculated for each temperature T using the minimum, mean, and maximum values of N_e as given in Table 4⁴. This was done for $R = 1, 50,$ and 215 . With this procedure, we found a relation between C_e and T as shown in Fig. 3. The full, dashed, and dashed dotted lines represent the results for the mean, minimum, and maximum values of N_e . The quadrangle A, B, C, D defines the area in the C_e – T plane for which the solutions of the Eqs. (9) and (10) would agree with the observational data.

Points A, B, C, D, and M are characterized by their coordinates C_e and T in the C_e – T plane. These are presented in Table 5, together with the corresponding values of the critical velocity v_c and radius r_c . At point M, all three full lines are closest to each other. Hence, the solution of Eqs. (9) and (10) connected with this point M should be considered as the best solution that agrees best with the observations. In the C_e – T plane, point M is given by $C_e = 9.127 \times 10^{34} \text{ s}^{-1}$ and $T = 1.18 \text{ MK}$. Because of $N_e = 1.12 N_p$ (see Sect. 2), C_e is related to C_p by $C_p = 0.893 C_e = 8.149 \times 10^{34} \text{ s}^{-1}$. This value for C_p agrees with PSP observations (see Fig. 2). The radial behaviours of the electron number density N_e and the proton (or solar wind) velocity v_p determined in this way are depicted as full lines in Figs. 4 and 5, respectively, and are listed numerically in Table 8.

The solution of point B represents the solution of Eqs. (9) and (10) with respect to the minimum of the electron number density, that is, it connects the electron number density $N_e = 4.311 \times 10^8 \text{ cm}^{-3}$ at $R = 1$ with $N_e = 4.453 \text{ cm}^{-3}$ at $R = 215$. It is drawn as the dashed line in Fig. 4. In contradiction to point

B, point D corresponds to the solution of Eqs. (9) and (10) for the maximum of the electron number density, that is, it connects the electron number density $N_e = 1.044 \times 10^9 \text{ cm}^{-3}$ at $R = 1$ with $N_e = 7.467 \text{ cm}^{-3}$ at $R = 215$. It is drawn as the dash-dotted line in Fig. 4.

With respect to the solar wind speed, the solution corresponding to point A represents the minimum of the solar wind speed, that is, $v_p = 0.1301 \text{ km s}^{-1}$ and $v_p = 484 \text{ km s}^{-1}$ at $R = 1$ and $R = 215$, respectively. It is drawn as the dashed line in Fig. 5. The solution corresponding to point C is connected with the maximum of the solar wind speed, that is, $v_p = 0.5541 \text{ km s}^{-1}$ and $v_p = 533 \text{ km s}^{-1}$ at $R = 1$ and $R = 215$, respectively. It is shown as the dashed-dotted line in Fig. 5.

4. Heliospheric magnetic field model

Banaszkiewicz et al. (1998) presented a global magnetic field model of the quiet heliosphere. It consists of a superposition of the magnetic field of the dipole and quadrupole of the quiet Sun and that of the heliospheric current sheet, which is considered to be azimuthal. It represents an extension of the dipole plus current sheet (DCS) model (Glessen & Axford 1974, 1976) by including the quadrupole moment of the quiet Sun. Therefore, it is called dipole plus quadrupole plus current sheet (DQCS) model. Because this is in cylindrical symmetry, the magnetic field is described in cylindrical coordinates. The radial and vertical components of the magnetic field given in Gauss are expressed by

$$\frac{B_r}{M} = \frac{3\rho z}{R^5} + \frac{15Q}{8} \cdot \frac{\rho z}{R^7} + \frac{K}{a} \cdot \frac{\rho}{[(|z| + a)^2 + \rho^2]^{3/2}} \quad (12)$$

and

$$\frac{B_z}{M} = \frac{2z^2 - \rho^2}{R^5} + \frac{3Q}{8} \cdot \frac{(8z^4 + 3\rho^4 - 2\rho^2 z^2)}{R^9} + \frac{K}{a} \cdot \frac{(|z| + a)}{[(|z| + a)^2 + \rho^2]^{3/2}}, \quad (13)$$

respectively (see Eqs. (1) and (2) in Banaszkiewicz et al. 1998). Here, the coordinates R , ρ , and z are given in solar radii. ρ denotes the radial distance from the centre of the Sun in the ecliptic plane. The z -axis with its coordinate z is directed perpendicular to the ecliptic plane. Hence, the complete distance R from the centre of the Sun in the heliosphere is given by $R^2 = \rho^2 + z^2$. The constants K , Q , and a are chosen in such a way that the last closed field line intersects the Sun at 60° , leading to $K = 1$, $Q = 1.5$, and $a = 1.538$ (Banaszkiewicz et al. 1998). The parameter M is fixed by the radial magnetic field component at 1 AU. In the ecliptic plane, that is, at $z = 0$, Eqs. (12) and (13) are reduced to

$$\frac{B_r}{M} = \frac{K}{a} \cdot \frac{\rho}{[a^2 + \rho^2]^{3/2}} \quad (14)$$

and

$$\frac{B_z}{M} = -\frac{1}{\rho^3} + \frac{9Q}{8} \cdot \frac{1}{\rho^5} + \frac{K}{[a^2 + \rho^2]^{3/2}} \quad (15)$$

because of $R = \rho$. In the limit $\rho \rightarrow \infty$, Eqs. (14) and (15) provide $B_r/M = (K/a\rho^2)$ and $B_z/M = (K-1)/\rho^3 = 0$ because $K = 1$, respectively. Thus, the component B_z vanishes for $\rho \rightarrow \infty$, as expected. Hence, the radial component is described by

$$B_r = B_0 \cdot \frac{\rho}{[a^2 + \rho^2]^{3/2}} \quad (16)$$

with $B_0 = (K \cdot M)/a$.

⁴ If a quantity X is given by its mean value \bar{X} and its standard deviation σ_X , here, $\min(X)$, $\text{mean}(X)$, and $\max(X)$ are defined by $\min(X) = \bar{X} - \sigma_X$, $\text{mean}(X) = \bar{X}$, and $\max(X) = \bar{X} + \sigma_X$, respectively.

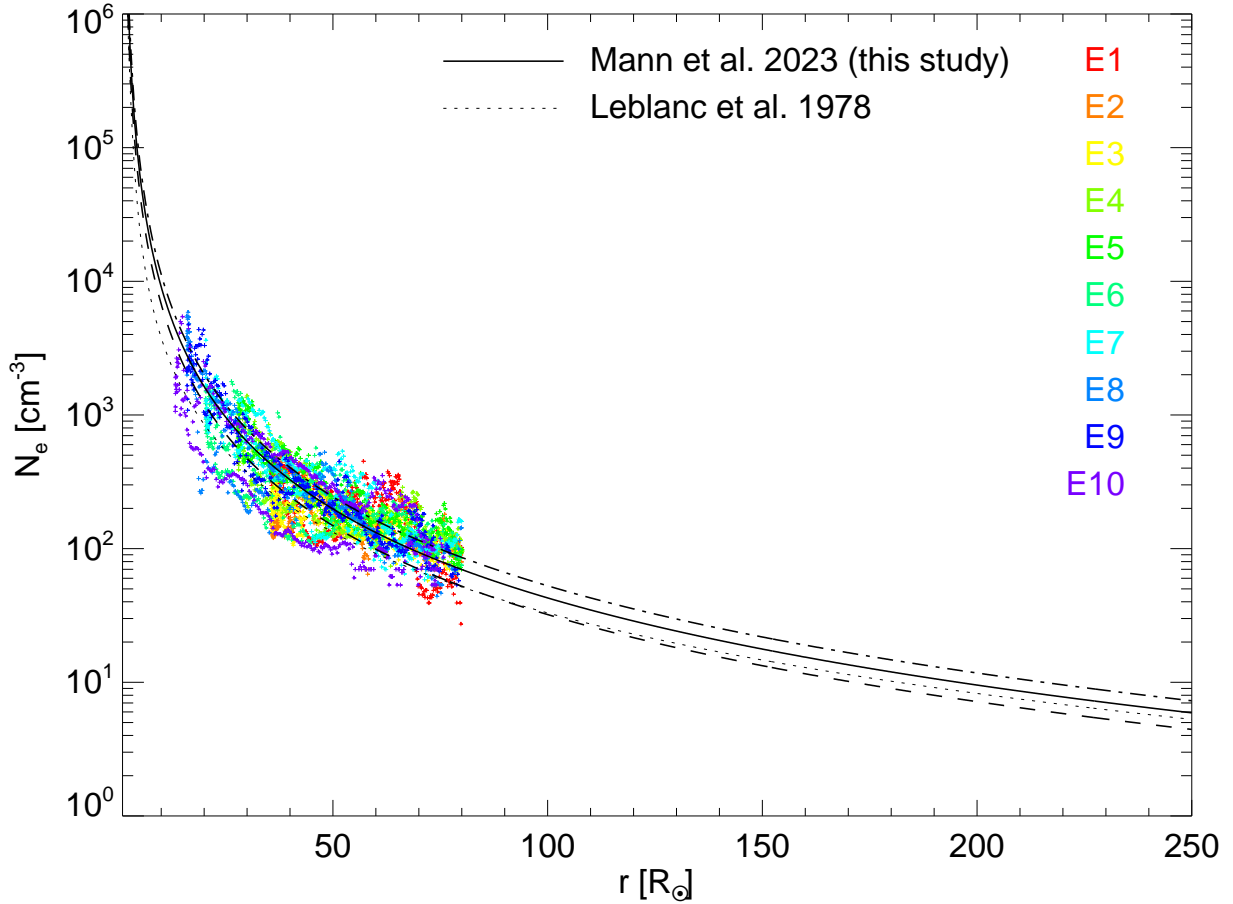


Fig. 4. As in Fig. 2, but showing the electron number density N_e as a function of heliocentric distance r . N_e was derived from PSP FIELDS data using quasi-thermal noise spectroscopy. The radial behaviour of the electron number density according to the model presented in Sect. 3 (see Table 4) is indicated as the solid line. For comparison, the dotted line represents the empirical model by Leblanc et al. (1998).

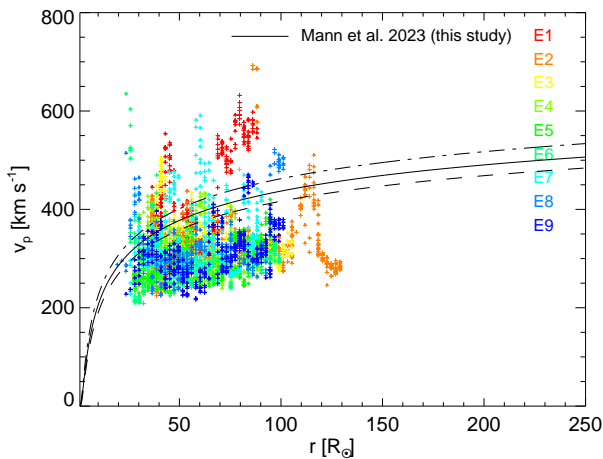


Fig. 5. As in Fig. 4, but showing the radial proton velocity v_p as measured by the SWEAP instrument as a function of heliocentric distance r . The radial behaviour of the proton speed according to the model presented in Sect. 3 (see Table 4) is plotted as the solid line.

The parameter B_0 is fixed by the in situ measurements of the magnetic field as given in Table 3. The radial component of the magnetic field B_r varies over a broad range (see Table 3 and Fig. 6). By means of Eq. (16), the quantities $\min(B_0)$, $\text{mean}(B_0)$, and $\max(B_0)$ were determined independently by the radial mag-

netic field B_r (see footnote 4) at $r/R_\odot = 30, 50, 70$, and 215 (see Table 6) and were subsequently averaged over these distances (see the bottom line in Table 6). Then, taking the averaged values for B_0 , the radial component of the magnetic field was varied in the range 0.78–2.51 nT at 1 AU ($=215 R_\odot$). This agrees with the observations (see Table 3).

According to Eqs. (14) and (15), the radial component B_r and the z -component B_z were calculated in the range $1-5 R_\odot$ as presented in Table 7. Tables 7 and 8 reveal that the magnetic field of the quiet Sun is predominantly radial beyond a distance of $1.4 R_\odot$ from the centre of the Sun (see Table 7). The interaction of the solar wind with the magnetic field lines of the rotating Sun leads to the formation of the Parker spiral (Parker 1958) in the heliosphere. Hence, the total magnetic field strength in the ecliptic plane can be expressed by

$$B_{\text{tot}}(r) = B_r(r) \cdot \sqrt{1 + \left(\frac{\Omega_\odot r}{v_p}\right)^2} = B_r(r) \cdot \sqrt{1 + \left(\frac{v_\odot}{v_p} \cdot \frac{r}{R_\odot}\right)^2} \quad (17)$$

(see Eq. (4.6) in Mariani & Neubauer 1990) with $v_\odot = \Omega_\odot R_\odot$. The solar rotational period is $T_\odot = 24.5$ days $= 2.117 \times 10^6$ s in the equatorial region, leading to $\Omega_\odot = 2\pi/T_\odot = 2.968 \times 10^{-6}$ s $^{-1}$ and $v_\odot = 2.065$ km s $^{-1}$. Equation (17) allows us to calculate the radial dependence of B_r , which is shown as the full line in Fig. 6 using $B_0 = 76\,000$ nT.

Table 8 summarizes our model results. It lists the radial dependency (r/R_\odot) of the electron density, N_e , the solar wind

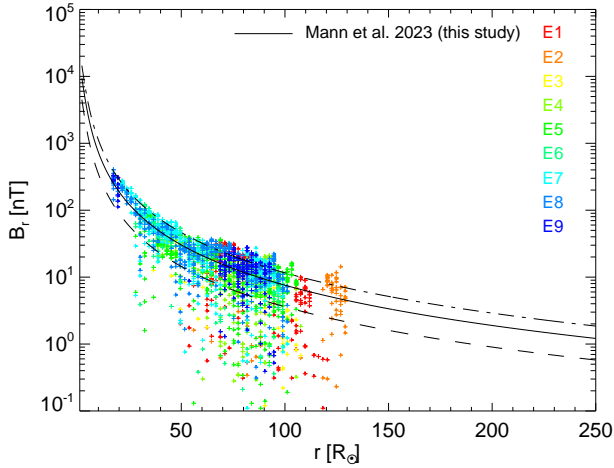


Fig. 6. As in Fig. 4, but showing the field strength of the radial component of the magnetic field B_r , as measured by the FIELDS instrument as a function of heliocentric distance r . The radial behaviour of B_r according to the model presented in Sect. 3 (see Table 4) is plotted as the solid line.

Table 6. Minimum, mean, and maximum value of the parameter B_0 of Eq. (16) as determined at $r/R_\odot = 30, 50, 70,$ and 215 according to Table 3.

r/R_\odot	Min (B_r) [nT]	Mean (B_r) [nT]	Max (B_r) [nT]
30	46 200	77 700	109 200
50	44 800	79 600	114 400
70	28 900	74 500	102 000
215	24 500	72 100	119 700
\emptyset	36 100	76 000	115 900

speed, v_p , the radial and total magnetic field strength, B_r and B_{tot} , and the Alfvén speed, v_A , in the radial range of $1\text{--}250 R_\odot$ ($2\text{--}250 R_\odot$ for the magnetic parameters). An extended electronic version of the table that lists the model results for all radial steps of $0.1 R_\odot$ is available at the CDS.

5. Discussion

In Sect. 3, Eqs. (9) and (10) were solved numerically. As a result, a solution was found for a specific choice of the parameters, as described in the last paragraph of Sect. 3. The second and third columns of Table 8 show the electron number densities N_e and solar wind (or proton) velocities v_p in the range $1\text{--}250 R_\odot$, respectively. The radial evolution of both quantities is shown as solid lines in Figs. 4 and 5.

In Fig. 4, our modelled electron number densities are compared to the values derived from PSP FIELDS data using quasi-thermal noise spectroscopy (see Moncuquet et al. 2020). Because this method does not work properly for low electron densities because the Debye length exceeds the length of the FIELDS antennas, we considered derived densities inside a heliocentric radial distance of $80 R_\odot$. For comparison, we also plot the model by Leblanc et al. (1998). The figure reveals that the special solutions of Eqs. (9) and (10) agree well with the observations of PSP and the empirical model by Leblanc et al. (1998) according to Eq. (7). The PSP measurements vary beyond our numerical solutions. This can be explained in the following

Table 7. Modelled magnetic field parameters as a function of radial distance in the solar corona.

r/R_\odot	B_r [nT]	B_z [nT]	$ B_z /B_r$
1.0	12 310	99 303	8.067
1.2	12 285	27 275	2.228
1.4	11 828	7072	0.598
1.6	11 124	967	0.087
1.8	10 308	-797	0.077
2.0	9465	-1169	0.124
3.0	5950	-467	0.078
4.0	3.863	-150	0.039
5.0	2654	-55	0.021

Notes. The table shows the radial component B_r and the z -component B_z according to Eqs. (14) and (15), respectively, and the ratio $|B_z|/B_r$.

Table 8. Radial behaviour of the electron number density N_e (the proton number density can be calculated by $N_p = 0.9 N_e$; see Sect. 2), solar wind (or proton) velocity v_p , the radial component of the magnetic field B_r , the total magnetic field strength B_{tot} (see Eq. (17)), and the Alfvén speed v_A (see Eq. (19)).

r/R_\odot	N_e [cm ⁻³]	v_p [km s ⁻¹]	B_r [nT]	B_{tot} [nT]	v_A [km s ⁻¹]
1.0	7.17×10^8	0.261	–	–	–
1.1	2.60×10^8	0.594	–	–	–
1.2	1.12×10^8	1.16	–	–	–
1.3	5.46×10^7	2.03	–	–	–
1.4	2.96×10^7	3.22	–	–	–
1.5	1.74×10^7	4.78	–	–	–
1.6	1.09×10^7	6.69	–	–	–
1.8	5.02×10^6	11.5	–	–	–
2.0	2.69×10^6	17.4	9442	9704	122
2.5	8.58×10^5	34.9	7495	7577	169
3.0	3.89×10^5	53.4	5936	5976	198
4.0	1.33×10^5	87.8	3853	3870	219
5.0	6.42×10^4	116	2648	2658	216
6.0	3.70×10^4	140	1914	1922	206
8.0	1.65×10^4	177	1122	1127	181
10.0	9.10×10^3	205	732	736	159
12.0	5.70×10^3	228	514	517	141
14.0	3.88×10^3	246	380	383	127
16.0	2.80×10^3	261	292	294	115
20.0	1.63×10^3	286	188	190	96.9
25.0	9.66×10^2	310	121	122	81.2
30.0	6.32×10^2	329	83.1	85.4	70.0
40.0	3.28×10^2	357	47.3	48.5	55.3
50.0	1.98×10^2	378	30.3	31.4	46.0
60.0	1.32×10^2	394	21.0	22.1	39.6
70.0	9.37×10^1	407	15.5	16.4	35.0
80.0	6.98×10^1	419	11.8	12.7	31.4
100.0	4.28×10^1	437	7.58	8.38	26.4
120.0	2.83×10^1	452	5.19	5.92	23.0
160.0	1.54×10^1	474	2.96	3.61	19.0
200.0	9.53	490	1.90	2.48	16.6
215.0	8.16	496	1.64	2.20	15.9
250.0	5.91	506	1.21	1.73	14.7

Notes. An extended electronic version of the table is available at the CDS.

manner: In our approach, we took the standard deviations of the electron number density into account, leading to three solutions of the mean, minimum, and maximum case. Thus, we did not include the total minimum and total maximum of the electron number density at radial distances of $1 R_\odot$, $50 R_\odot$, and $215 R_\odot$ from the centre of the Sun, that is, we did not consider the whole variations of the electron number density⁵. In Fig. 5 we compare the model to the proton speeds as measured by SWEAP on board PSP. Here, the deviations of the measured values from the modelled ones are greater than in the case of the electron number density (see Fig. 4).

For the coronal height range, Fig. 1 shows several remote-sensing measurements of the electron number density in quiet equatorial regions. The mean radial evolution of the electron number density $N_e(r)$ (see Table 8) is plotted as the solid line in Fig. 1. In the distance range $R = 1-2$, it is evident that the density model presented in Sect. 3 is consistent with the coronal observations. As discussed in the second paragraph of Sect. 3, Eqs. (9) and (10) can be solved analytically for the corona. For electrons, this gives

$$N_e(r) = N_{e,\odot} \cdot \exp\left(11.35 \cdot \left[\frac{R_\odot}{r} - 1\right]\right) \quad (18)$$

with $N_{e,\odot} = 7.17 \times 10^8 \text{ cm}^{-3}$ and $2 r_c/R_\odot = 11.14$, which results from adopting the parameters given in the third paragraph of Sect. 3. It should be emphasized that this analytical formula describes the radial density in the corona and near-Sun interplanetary space well up to a distance of $3 R_\odot$ from the centre of the Sun. For illustration, Eq. (18) provides $N_e = 4.267 \times 10^5 \text{ cm}^{-3}$ at $r = 3 R_\odot$, whereas the exact solution yields $N_e = 3.92 \times 10^5 \text{ cm}^{-3}$ (see Table 8) at the same radial distance.

After considering the electron density and solar wind speed, we show in Fig. 6 the radial dependence on the radial magnetic field strength B_r according to the values given in Table 8. Again, the comparison to the PSP measurements obtained by FIELDS reveals a good agreement between our model and the measured field strengths.

For the corona, Table 7 lists the radial dependence of B_r and B_z according to Eqs. (16) and (17), and the ratio B_z/B_r . The radial component B_r dominates component B_z beyond a radial distance of $1.4 R_\odot$. Below $1.4 R_\odot$, the dipole and quadrupole part of the magnetic field are the dominant parts of the magnetic field.

The Parker spiral is formed by the interaction of the magnetic field with the solar wind and with the rotating Sun. The fifth column of Table 8 presents the values of the total magnetic field B_{tot} as defined by Eq. (17).

The radial dependence of the Alfvén speed v_A can now be determined with the knowledge of the radial evolution of the density and magnetic field according to

$$v_A = \frac{B_{\text{tot}}}{\sqrt{4\pi\tilde{\mu}Nm_p}} = \frac{B_{\text{tot}}}{\sqrt{4\pi \cdot 1.11 \cdot N_e m_p}} \quad (19)$$

(m_p is the proton mass) with $\tilde{\mu} = 0.57$ and $N = 1.95 N_e$ (see the third paragraph in Sect. 2). The values of the Alfvén velocity as derived from our model are listed in the Table 8. While the model by Banaszekiewicz et al. (1998) presents a global magnetic field model of the heliosphere, this is not appropriate for describing the magnetic field in the low corona, which is characterized by a mixture of open and closed magnetic field lines (see

⁵ The same is also the case for all other quantities (e.g. V_p , C_p , C_e , B_r , and B_{tot}).

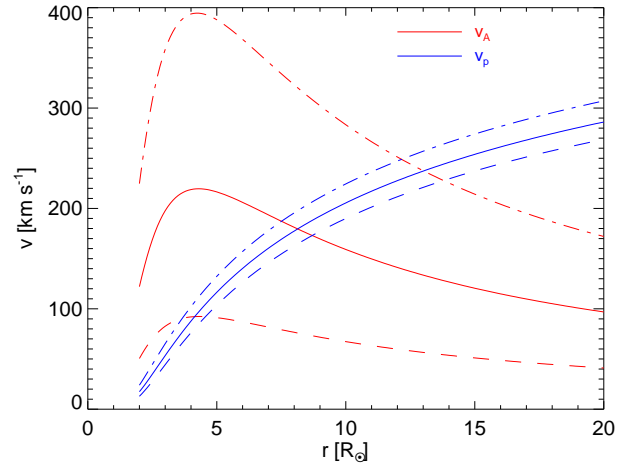


Fig. 7. Radial behaviour of the local Alfvén velocity for the mean (full line), minimum (dashed line), and maximum (dash-dotted line) case. For comparison, the radial behaviour of the solar wind speed is also shown in blue for the mean (full line), minimum (dashed line), and maximum (dash-dotted line) case.

Aschwanden 2005). The Alfvén velocity was therefore only calculated for radial distances beyond $2.0 R_\odot$ by means of Eq. (19). This was done for the mean, minimum, and maximum case as defined by

$$\text{mean}[v_A(r)] = \frac{\text{mean}[B_{\text{tot}}(r)]}{\sqrt{4\pi \cdot 1.11 m_p \cdot \text{mean}[N_e(r)]}} \quad (20)$$

$$\text{min}[v_A(r)] = \frac{\text{min}[B_{\text{tot}}(r)]}{\sqrt{4\pi \cdot 1.11 m_p \cdot \text{max}[N_e(r)]}} \quad (21)$$

and

$$\text{max}[v_A(r)] = \frac{\text{max}[B_{\text{tot}}(r)]}{\sqrt{4\pi \cdot 1.11 m_p \cdot \text{min}[N_e(r)]}}, \quad (22)$$

respectively. Their radial behaviour is depicted as the full, dashed, and dash-dotted line for the mean, minimum, and maximum case in Fig. 7, respectively. The local Alfvén velocity increases in the near-Sun interplanetary space and reaches a maximum of 219 km s^{-1} , 92.1 km s^{-1} , and 392 km s^{-1} at $4 R_\odot$ in the mean, minimum, and maximum case according to Eqs. (20)–(22), respectively. Mann et al. (1999b, 2003) have already reported a local maximum like this of the Alfvén speed in the near-Sun interplanetary space. Beyond $4 R_\odot$, it decreases to 15.9 km s^{-1} , 6.79 km s^{-1} , and 27.9 km s^{-1} at 1 AU for the mean, minimum, and maximum case, respectively. For comparison, the radial behaviours of the solar wind speeds are also presented in Fig. 7. The Alfvénic point (or surface) is defined as the location at which the solar wind speed is equal to the local Alfvén velocity. During the eighth encounter on April 28, 2021, PSP entered regions in which the local Alfvén velocity exceeded the solar wind speed during three intervals (Kasper et al. 2021). This occurred at radial distances in the range of $16.0-19.8 R_\odot$. The ratios v_p/v_A were in the range $0.49-0.88$ (see Table 1 in Kasper et al. 2021). Figure 7 reveals that the solar wind speed can exceed the local Alfvén speed in a broad radial range of $3.6-13.7 R_\odot$ according to our model. The Alfvénic points in the range $16.0-19.8 R_\odot$ as measured by PSP are not so far away from the points predicted by our model, however. Kasper et al. (2021) argued that this sub-Alfvénic wind might correspond to solar wind originating in a pseudo-streamer structure. Our model

should be understood as a long-term average model of the heliosphere and is not intended to model the full variability of solar wind conditions induced by complex coronal structures.

6. Summary

The model presented in this paper agrees well with remote-sensing and in situ measurements of the plasma density and magnetic field strength in the heliosphere. In addition to being consistent with both coronal observations and measurements at 1 AU, it reproduces recent data from the inner heliosphere provided by the PSP mission. In the model, the heliosphere is considered as a stationary and homogeneous medium, which is an approximation. The heliosphere is spatially structured, which includes coronal holes, streamers, or fast and slow wind streams (see Priest 1982; Aschwanden 2005). Furthermore, the heliosphere varies on a long timescale with the 11-year solar cycle, while on shorter timescales, there are propagating features such as travelling CMEs, propagating shocks, and CIRs (see Schwenn 1990). Kinetic plasma processes play an important role in the corona and solar wind (see Marsch 2006). They cause macroscopic phenomena such as the heating of the corona and the acceleration of the solar wind by the Alfvén wave pressure (Hackenberg et al. 2000; Tu & Marsch 2001a,b; Vocks & Marsch 2001; Vocks & Mann 2003; Hofmeister et al. 2022).

Considering these complications, it is still necessary to have a simple but physically justified model of the plasma density and magnetic field in the heliosphere. For instance, a model like this is necessary for evaluating the propagation of CMEs through the heliosphere (which has strong implications for space weather) or for studying the propagation of interplanetary electron beams by inferring their kinematics from the analysis of associated type III radio bursts. The model presented in this paper fulfils these criteria. The predicted radial behaviour of the density, the magnetic field, and the Alfvén speed is consistent with observations from the coronal base up to 1 AU. While the model does not account for spatial and temporal variations of the heliosphere, it should be considered as a long-term average global model. We emphasize that the model we presented has a physical basis in terms of Parker’s wind equation (Parker 1958) and the DQCS-model by Banaszkiwicz et al. (1998).

Acknowledgements. Parker Solar Probe was designed, built, and is now operated by the Johns Hopkins Applied Physics Laboratory as part of NASA’s Living with a Star (LWS) program (contract NNN06AA01C). Support from the LWS management and technical team has played a critical role in the success of the Parker Solar Probe mission. Thanks to the FIELDS team for providing data (PI: S. D. Bale, UC Berkeley). Thanks to the Solar Wind Electrons, Alphas, and Protons (SWEAP) team for providing data (PI: J. Kasper, BWX Technologies). We thank Michel Moncuquet (PSP/Fields Co-I) for providing QTN density data. We acknowledge use of NASA/GSFC’s Space Physics Data Facility’s OMNIWeb service, and OMNI data. The work of A. P. Rouillard was funded by the ERC SLOW SOURCE project (SLOW SOURCE-DLV-819189).

References

Alvarez, H., & Haddock, F. T. 1973, *Sol. Phys.*, 29, 197

- Aschwanden, M. J. 2005, *Physics of the Solar Corona* (Chichester: Springer)
- Aschwanden, M. J., Newmark, J. S., Delaboudiniere, J.-P., et al. 1999, *ApJ*, 515, 842
- Badman, S. T., Carley, E., Canizares, L. A., et al. 2022, *ApJ*, 938, 95
- Bale, S. D., Goetz, K., Harvey, P. R., et al. 2016, *Space Sci. Rev.*, 204, 49
- Balogh, A., Smith, E. J., Tsurutani, B. T., et al. 1995, *Science*, 268, 1007
- Banaszkiewicz, M., Axford, W. I., & McKenzie, J. F. 1998, *A&A*, 337, 940
- Baumbach, S. 1937, *Astron. Nachr.*, 263, 121
- Bird, M. K., & Edenhofer, P. 1990, *Remote Sensing observations of the Solar Corona* (Berlin, Heidelberg: Springer-Verlag), 13
- Bird, M. K., Volland, H., Paetzold, M., et al. 1994, *ApJ*, 426, 373
- Bougeret, J.-L., King, J. H., & Schwenn, R. 1984, *Sol. Phys.*, 90, 401
- Bougeret, J.-L., Kaiser, M. L., Kellogg, P. J., et al. 1995, *Space Sci. Rev.*, 71, 231
- Brosius, J. W., Davilla, J. M., Thomas, R. J., & Monsignore-Fossi, B. C. 1996, *ApJS*, 106, 143
- Del Zanna, G., & Mason, H. E. 2003, *A&A*, 406, 1089
- Dulk, G. A., & McLean, D. J. 1978, *Solar Phys.*, 57, 279
- Erickson, W. C. 1964, *ApJ*, 139, 1290
- Gallagher, P. T., Mathioudakis, M., Keenan, F. P., et al. 1999, *ApJ*, 524, L133
- Glessen, L. J., & Axford, W. I. 1974, *EOS Trans. AGU*, 55, 404
- Glessen, L. J., & Axford, W. I. 1976, *J. Geophys. Res.*, 81, 3403
- Gritton, L., Rouillard, A. P., Poirier, N., et al. 2021, *ApJ*, 910, 63
- Hackenberg, P., Marsch, E., & Mann, G. 2000, *A&A*, 360, 1139
- Horbury, T. S., O’Brien, H., Blazquez, I. C., et al. 2020, *A&A*, 642, A9
- Hofmeister, S. J., Asvestavi, E., Guo, J., et al. 2022, *A&A*, 659, A190
- Issautier, K., Meyer-Vernet, N., Moncuquet, M., & Hoang, S. 1997, *Sol. Phys.*, 172, 335
- Kasper, J. C., Abiad, R., Austin, G., et al. 2016, *Space Sci. Rev.*, 204, 131
- Kasper, J. C., Klein, K. G., Lichko, E., et al. 2021, *Phys. Rev. Lett.*, 127, 255101
- Koutchmy, S. 1994, *Adv. Space Res.*, 14, 243
- Koutchmy, S., & Livshits, M. 1992, *Space Sci. Rev.*, 61, 393
- Landi, E., & Landini, M. 1998, *A&A*, 340, 265
- Lin, R. P., Anderson, K. A., Ashford, S., et al. 1995, *Space Sci. Rev.*, 71, 246
- Leblanc, Y., Leroy, J. L., & Pecantet, P. 1973, *Sol. Phys.*, 31, 343
- Leblanc, Y., Dulk, G. A., & Bougeret, J.-L. 1998, *Sol. Phys.*, 183, 165
- Mann, G., Jansen, F., MacDowall, M. J., Kaiser, M. L., & Stone, R. G. 1999a, *A&A*, 348, 614
- Mann, G., Aurass, H., Klassen, A., Estel, C., & Thompson, B. J. 1999b, in Proc. 8th SOHO Workshop, ed. B. Kaldeich-Schürmann, *ESA SP-446*, 477
- Mann, G., Klassen, A., Aurass, H., & Klassen, H.-T. 2003, *A&A*, 400, 329
- Mariani, F., & Neubauer, F. M. 1990, *The Interplanetary Magnetic Field* (Berlin, Heidelberg: Springer-Verlag), 13
- Marsch, E. 2006, *Liv. Rev. Sol. Phys.*, 3, 100
- Moncuquet, M., Meyer-Vernet, N., Issautier, K., et al. 2020, *ApJS*, 246, 44
- Morgan, H. 2021, *ApJ*, 922, 165
- Newkirk, G. A. 1961, *ApJ*, 133, 983
- Owens, M. J., & Forsyth, R. J. 2013, *Living Rev. Solar Phys.*, 10, 5
- Pätzold, M., Bird, M. K., Volland, H., et al. 1987, *Sol. Phys.*, 109, 91
- Papitashvili, N. E., & King, J. H. 2020, “OMNI Daily Data”, *NASA Space Physics Data Facility*, <https://doi.org/10.48322/5fmx-hv56>
- Parker, E. N. 1958, *ApJ*, 128, 664
- Porsche, H. 1977, *J. Geophys. Res.*, 42, 551
- Priest, E. R. 1982, *Solar Magnetohydrodynamics* (Dordrecht: Reidel)
- Reid, H. A. S., & Ratcliffe, H. 2014, *Res. Astron. Astrophys.*, 14, 773
- Rouillard, A. P., Poirier, N., Laverra, M., et al. 2020, *ApJS*, 246, 72
- Saito, K., Poland, A. J., & Munro, R. H. 1977, *Sol. Phys.*, 55, 121
- Schwenn, R. 1990, *Large-Scale Structures of the Interplanetary Medium* (Berlin, Heidelberg: Springer-Verlag), 99
- Stone, E. C., Frandsen, A. M., & Newwaldt, R. A. 1998, *Space Sci. Rev.*, 86, 1
- Tu, C.-Y., & Marsch, E. 2001a, *A&A*, 368, 1071
- Tu, C.-Y., & Marsch, E. 2001b, *J. Geophys. Res.*, 106, 8233
- Van de Hulst, H. C. 1950, *Bull. Astron. Inst. Neth.*, 11, 135
- Vocks, C., & Marsch, E. 2001, *Geophys. Res. Lett.*, 28, 1817
- Vocks, C., & Mann, G. 2003, *ApJ*, 593, 1134
- Vršnak, B., Žic, T., Vrbanc, D., et al. 2013, *Sol. Phys.*, 285, 295
- Wild, J. P. 1950, *Austr. J. Sci. Res. Ser. A*, 3, 541
- Yang, Z., Bethge, C., Tian, H., et al. 2020, *Science*, 369, 694
- Zucca, P., Carley, E. P., Bloomfield, D. S., & Gallagher, P. 2014, *A&A*, 564, A47